Check for updates

Ag₃PO₄/CoFe₂O₄ magnetic nanocomposite: synthesis, characterization and applications in catalytic reduction of nitrophenols and sunlight-assisted photocatalytic degradation of organic dye pollutants

Eslam Abroushan, Saeed Farhadi [ID] * and Abedien Zabardasti

A novel magnetically recyclable Ag₃PO₄/CoFe₂O₄ nanocomposite (containing 30 wt%. CoFe₂O₄) was synthesized by a facile hydrothermal method. The composition and microstructure of the nanocomposite was fully characterized by X-ray diffraction (XRD), Fourier transform infrared spectroscopy (FTIR), UV-visible spectroscopy (UV-vis), field emission scanning electron microscopy (FESEM)-energy dispersive X-ray (EDX) spectroscopy, transmission electron microscopy (TEM), and a vibrating sample magnetometer (VSM). Thereafter, the catalytic performance of the Ag₃PO₄/CoFe₂O₄ nanocomposite was investigated. The Ag₃PO₄/CoFe₂O₄ nanocomposite showed high efficiency for the degradation of methylene blue (MB) and Rhodamine B (RhB) dyes under direct sunlight irradiation. The photocatalytic activity of Ag₃PO₄/CoFe₂O₄ under sunlight irradiation was almost 1.5 and 4.7 times as high as those of the pure Ag₃PO₄ and CoFe₂O₄, respectively. The enhancement of sunlight photocatalytic activity in Ag₃PO₄/CoFe₂O₄ should be assigned to the effective separation and transfer of photogenerated charges originating from the well-matched overlapping band-structures. Trapping experiments indicated that superoxide anion ($\cdot O_2^-$) radicals were the main reactive species for dye degradation in the present sonocatalytic system. A proposed mechanism for the enhanced photocatalytic activity is also discussed based on the experimental results. In addition, the catalytic activity of the nanocomposite in the reduction of nitrophenols by using NaBH₄ was evaluated. The results showed that Ag₃PO₄/CoFe₂O₄ exhibited the best performance in the reduction of 4-nitrophenol (4-NP) and 2-nitrophenol (2-NP) and revealed 100% conversion into the corresponding amino derivatives within 24–46 min with rate constant equal to 0.0714 min⁻¹ and 0.0329 min⁻¹, respectively. Moreover, due to the existence of the CoFe₂O₄, the Ag₃PO₄/CoFe₂O₄ nanocomposite could be magnetically separated from the reaction mixture and reused without any change in structure.

1. Introduction

Solar energy is the most clean, abundant and renewable energy source. The energy from the sun that hits the earth for one hour is much more than that needed by human beings for one year.[1,2] It is well-known that the ultraviolet (UV) region occupies only approximately 4% of the entire solar spectrum, while 43% of the energy is that of visible light.[3,4] Therefore, the development of novel efficient photocatalysts, particularly visible light responsive catalysts, is necessary for the efficient utilization of solar energy in photocatalysis.[5–7] Developing a novel photocatalyst with efficient visible-light absorption and excellent stability remains a great challenge.

Among various photoactive materials, silver orthophosphate (Ag₃PO₄) has attracted considerable attention and found to be an excellent photocatalyst in visible light region because of its superior semiconductor property for directly splitting water, degrading organic contaminants and photodecomposition of organic dyes.[7,8] Ag₃PO₄ has a relatively narrow band gap (2.36–2.43 eV) and is thus active under visible-light irradiation ($\lambda < 530$ nm).[9] Unfortunately, Ag₃PO₄ suffers from the structural stability issues because the photocatalytic process is usually accompanied by the transformation of Ag⁺ into Ag⁰ in the absence of a sacrificial reagent. However, previous investigations have demonstrated that combining two or more semiconductors to fabricate an appropriate composite structure may be a good strategy.[10,11]

To date, many efforts had been tried, and some Ag₃PO₄-based hybrid composite, such as Ag₃PO₄/WO₃,[12] Ag₃PO₄/CeO₂,[13] Ag₃PO₄/(Cr)–SrTiO₃,[14,15] Ag₃PO₄/In(OH)₃,[16] BiOCl/Ag₃PO₄,[17]

Department of Chemistry, Lorestan University, Khoramabad 68151-44316, Iran. E-mail: sfarhadi1348@yahoo.com; Fax: +98-6633120611; Tel: +98-6633120618

$Ag_3PO_4/BiVO_4$,[18] g-C_3N_4/Ag_3PO_4,[19–21] $Ag/Ag_2S/Ag_3PO_4$,[22] Ag_3PO_4/ZnO,[23] Ag_3PO_4/SnO_2,[24] Ag_3PO_4/TiO_2,[25,26] AgX/Ag_3PO_4 (X = Cl, Br, I),[27,28] Ag_3PO_4/Nb_2O_5 [29] and CdS/Ag_3PO_4 [30] had been successfully synthesized, which showed enhanced photocatalytic stability and activity than pure Ag_3PO_4. But these composites are difficult to separate and recycle, seriously limiting their extensive application. Therefore, fabrication of well-defined and easy separated Ag_3PO_4-based photocatalysts from the suspended reaction system *via* a simple process remains to be a great challenge. To overcome this shortfall, coupling with magnetic materials is highly desirable. Magnetic based materials can be easily recovered by a magnet and can be reused for photocatalysis reaction several times without any appreciable reduction in photocatalytic efficiency.[31,32] Although, pure magnetic materials are easily recovered, their photocatalytic activities are very weak. They usually take long time to degrade the organic pollutant. Therefore, it is desirable to couple the magnetic photocatalyst with photocatalyst having high photocatalytic efficiency. Such composite photocatalysts can exhibit good magnet-controlled recyclability as well as superior photocatalytic activity with improved stability. In this regard, cubic $CoFe_2O_4$ is known to have high magnetic performance as well as excellent chemical stability. $CoFe_2O_4$ nanoparticles themselves have a strong magnetic property, and therefore, $CoFe_2O_4$ based composites can be magnetically separable in a suspension by virtue of their own magnetic properties without introduction of additional magnetic particles.

Considering the above, in the present work we have synthesized magnetically recyclable $Ag_3PO_4/CoFe_2O_4$ nanocomposite by a simple hydrothermal route. The visible light photocatalytic activity of the as-synthesized $Ag_3PO_4/CoFe_2O_4$ nanocomposite was evaluated for the degradation methylene blue (MB) and Rhodamine B (RhB) dyes under natural sunlight irradiation. In addition, the catalytic activity of this magnetic nanocomposite for the reduction of nitrophenols was investigated. The recycle experiments and possible photodegradation mechanism in $Ag_3PO_4/CoFe_2O_4$ system were also proposed.

2. Experimental

2.1. Materials

Cobalt(II) nitrate hexahydrate ($Co(NO_3)_2 \cdot 6H_2O$, 98%), iron(III) nitrate nanohydrate ($Fe(NO_3)_3 \cdot 9H_2O$, 98%), silver nitrate ($AgNO_3$, 98%), disodium hydrogen phosphate (Na_2HPO_4, 98.5%), sodium borohydride ($NaBH_4$, 98.5%), 2-nitrophenol (99%), 4-nitrophenol (98%), methylene blue (99%) and Rhodamine B (99%) were obtained from Merck chemical company and used as received without further purification.

2.2. Synthesis of $CoFe_2O_4$ nanoparticles

In a typical synthesis, 1.72 g of iron(III) nitrate nanohydrate ($Fe(NO_3)_3 \cdot 9H_2O$) and 0.62 g cobalt (II) nitrate hexahydrate ($Co(NO_3)_2 \cdot 6H_2O$) were dissolved in 25 mL of water by magnetic stirring for 30 min. After that, the mixture was adjusted to a pH of 12.0 with 6 M NaOH solution and stirred for 60 min, yielding a homogeneous emulsion. The resulting mixture was

transferred into a 50 mL Teflon-lined stainless steel autoclave and heated to 180 °C for 12 h. The reaction mixture was allowed to cool to room temperature and the precipitate was filtered, washed with distilled water five times, and dried in a vacuum oven at 60 °C for 12 h.

2.3. Synthesis of $Ag_3PO_4/CoFe_2O_4$ nanocomposite

The preparation of $Ag_3PO_4/CoFe_2O_4$ (30 wt%) nanocomposite was carried out as follows: in a typical experiment, 26 mg $CoFe_2O_4$ powder was added into 20 mL deionized water and sonicated for 10 min to get uniform dispersion. Then, 1.0 mL Na_2HPO_4 (0.15 mol L^{-1}) and 3.0 mL $AgNO_3$ (0.15 mol L^{-1}) aqueous solutions were added into the suspension and sonicated for 3 h. The dispersed mixture was added to a Teflon-lined stainless steel autoclave for hydrothermal treatment at 160 °C for 3 h. Then, the reaction mixture was allowed to cool to room temperature and the precipitate was filtered, washed with distilled water three times, and dried in an oven at 80 °C for 6 h. The exact content of $CoFe_2O_4$ in the nanocomposite was also confirmed by using ICP-AES. The $CoFe_2O_4$ content measured was 29.45 wt% which is in agreement with the theoretical amount (30 wt%). For comparison, pure Ag_3PO_4 was also prepared under the same conditions without adding $CoFe_2O_4$.

2.4. Characterization techniques

The XRD patterns of the samples were obtained on an X-ray diffractometer (PANalytical/X'Pert Pro MPD) using Ni-filtered Cu Kα radiation ($\lambda = 1.54059$ Å) radiation FT-IR spectra were recorded on a Schimadzu system FT-IR 160 spectrophotometer in transmission mode from 4000 to 400 cm^{-1} using KBr pellets. UV-vis spectra of samples (photocatalysts, nitrophenols and dyes) were analyzed at room temperature using a CARY 100 double beam spectrophotometer operated at a resolution of 2 nm with quartz cells with path length of 1 cm in the wavelength range of 200 to 750 nm. UV-visible DRS of the photocatalysts samples were recorded with a Shimadzu UV-2450 spectrophotometer over the spectral range 200–700 nm. The shape and morphology of samples were observed by a MIRA3 TESCAN scanning electron microscope (SEM) equipped with a link energy-dispersive X-ray (EDX) analyzer. The particle size was determined by a LEO-912AB transmission electron microscope (TEM) at an accelerating voltage of 80 kV. TEM samples were prepared by dropping the ethanol dispersion on a carbon coated copper grid. Magnetic measurements were carried out at room temperature using a vibrating sample magnetometer (VSM, Magnetic Daneshpajoh Kashan Co., Iran) with a maximum magnetic field of 10 kOe. The content of $CoFe_2O_4$ in the nanocomposite was determined by inductively coupled plasma atomic emission spectroscopy (ICP-AES, model OEC-730).

2.5. Catalytic reduction tests

In order to study the catalytic performance of the as-synthesized $Ag_3PO_4/CoFe_2O_4$ nanocomposite in reductive processes, the reduction of 4-nitrophenol (4-NP) to 4-aminophenol (4-AP) by excess $NaBH_4$ in aqueous solution was used as the model reaction. For the catalytic reduction tests, freshly prepared

aqueous solution of $NaBH_4$ (0.5 mL, 20 mM) was mixed with aqueous solution (3 mL, 0.2 mM) of 4-NP in the quartz cell (1.0 cm path length and 4 mL volume). The color of the solution immediately changed from yellow to colorless. Then, 5 mg of $Ag_3PO_4/CoFe_2O_4$ nanocatalyst was added into the solution. The progress of reduction was monitored by UV-vis spectrophotometry in a range of 200–550 nm, with cycling over an interval of 2 min at ambient temperature. The reduction of 2-nitrophenol (2-NP) to 2-aminophenol (2-AP) was also investigated under the same conditions.

2.6. Photocatalytic degradation tests

To evaluate the photocatalytic activity of the $Ag_3PO_4/CoFe_2O_4$ nanocomposite, the degradation of methylene blue (MB) and Rhodamine B (RhB) organics in water was studied under direct natural sunlight irradiation. The photocatalytic experiments were executed on the days of bright sunny light in between 10 am to 2 pm in the summer session of Khoramabad city, Lorestan province, western region of Iran and the average intensity of light measured was ~185 mW cm^{-2} (CHY 332, Digital Light Meter). In a typical photocatalytic reaction, 25 mg of $Ag_3PO_4/CoFe_2O_4$ nanocomposite was add to 50 mL of an aqueous solution of dye with initial concentration (C_0) of 15 mg L^{-1}. The mixture was kept in the dark for 30 min under continuous stirring to achieve the adsorption–desorption equilibrium of dye on the photocatalyst surface. Photocatalytic degradation was carried out by illuminating the suspension under natural sunlight. The degradation of dyes was monitored by UV-vis spectroscopy at different time intervals. For comparison, the photocatalytic activity of pure Ag_3PO_4 (15 mg) and $CoFe_2O_4$ (10 mg) were also investigated under the same conditions.

Various scavengers, including p-benzoquinone (BQ; 5 mmol L^{-1}), triethanolamine (TEA; 5 mmol L^{-1}), isopropyl alcohol (IPA; 5 mmol L^{-1}), KI (5 mmol L^{-1}) and $AgNO_3$ (Ag^+; 0.5 mmol L^{-1}), were added into the solution of MB to detect the active species generated in the photodegradation experimental process. The photocatalytic process was the same as that described in the above. To test the recyclability, the $Ag_3PO_4/CoFe_2O_4$ nanocomposite was separated with an external magnet after dye had been completely degraded and washed with deionized water three times before the next photocatalytic reaction.

3. Results and discussion

3.1. Characterization of $Ag_3PO_4/CoFe_2O_4$ nanocomposite

The XRD patterns of the as-prepared Ag_3PO_4, $CoFe_2O_4$, and $Ag_3PO_4/CoFe_2O_4$ nanocomposite are presented in Fig. 1. For the as-prepared Ag_3PO_4 sample in Fig. 1(a), it can be seen that all the diffraction peaks can be well indexed to a body-centered cubic phase (JCPDS no. 01-084-0192; space group, $P\bar{4}3n$; $a_0 = 6.0095$ Å) and no other features were observed. From the XRD Pattern of the as-prepared $CoFe_2O_4$ nanoparticles in Fig. 1(b), it is obvious that all the diffraction peaks match very well with standard data of $CoFe_2O_4$ (JCPDS no. 01-022-1086; space group, $Fd\bar{3}m$; $a_0 = 8.3919$ Å), and no trace of any impurity phase was

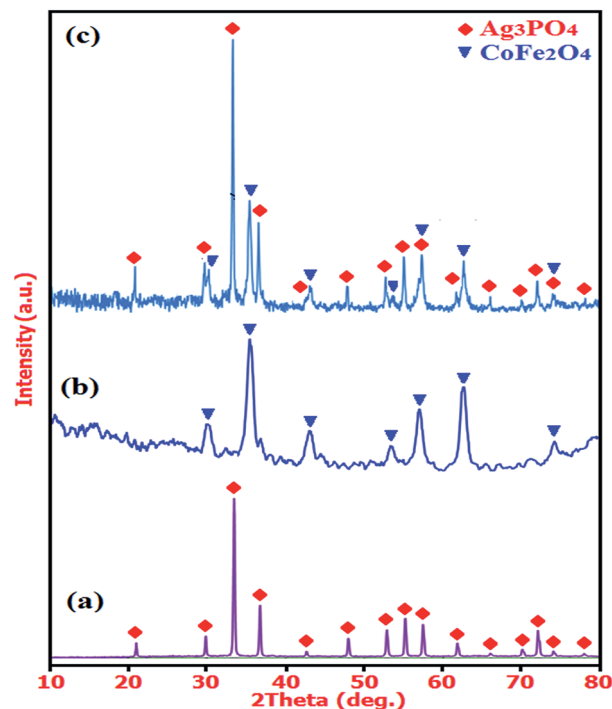**Fig. 1** XRD patterns of (a) Ag_3PO_4, (b) $CoFe_2O_4$ and (c) $Ag_3PO_4/CoFe_2O_4$ nanocomposite.

found. As observed in Fig. 1(c), the XRD pattern of composite sample exhibits diffraction peaks corresponding to both Ag_3PO_4 and $CoFe_2O_4$ and no other impure peaks can be observed, indicating that the sample is composed of Ag_3PO_4 and $CoFe_2O_4$ and the $Ag_3PO_4/CoFe_2O_4$ composite has been successfully prepared.

FT-IR spectra of the as-prepared Ag_3PO_4, $CoFe_2O_4$, and $Ag_3PO_4/CoFe_2O_4$ nanocomposite are indicated in Fig. 2. For Ag_3PO_4 sample in Fig. 2(a), the sharp peaks at $ca.$ 925 and 550 cm^{-1} are the characteristic asymmetric stretching and bending vibration of PO_4^{3-} groups, respectively.[33] In the case of $CoFe_2O_4$ (Fig. 2(b)), the two peaks in the range of 400 to 600 cm^{-1} are due to the Fe(III)–O and Co(II)–O bond of spinel-type oxide.[34–37] In the FT-IR spectrum of the $Ag_3PO_4/CoFe_2O_4$ sample in Fig. 2(a), the representative PO_4^{3-} group stretching vibration mode at 930 cm^{-1} is also observed besides the featured absorption bands of $CoFe_2O_4$ in the 400–600 cm^{-1} range. This is a good proof that $Ag_3PO_4/CoFe_2O_4$ nanocomposite was formed in the present study, as evidenced by the above XRD results. In all samples, the peaks at 1635 and 3350 cm^{-1} are attributed to the typical stretching vibrations of –OH group of adsorbed water.

Further investigation was carried out by energy dispersive X-ray spectroscopy (EDX) to characterize the composition of the as-prepared $Ag_3PO_4/CoFe_2O_4$ nanocomposite as shown in Fig. 3. It can be clearly seen that Co, O, Ag, Fe and P elements are all existed in the product, which is consistent with the results obtained from XRD patterns. The inset of Fig. 3 shows a representative SEM image of the nanocomposite with corresponding EDX elemental mappings. Brighter area in the elemental map indicates a higher concentration of the corresponding element
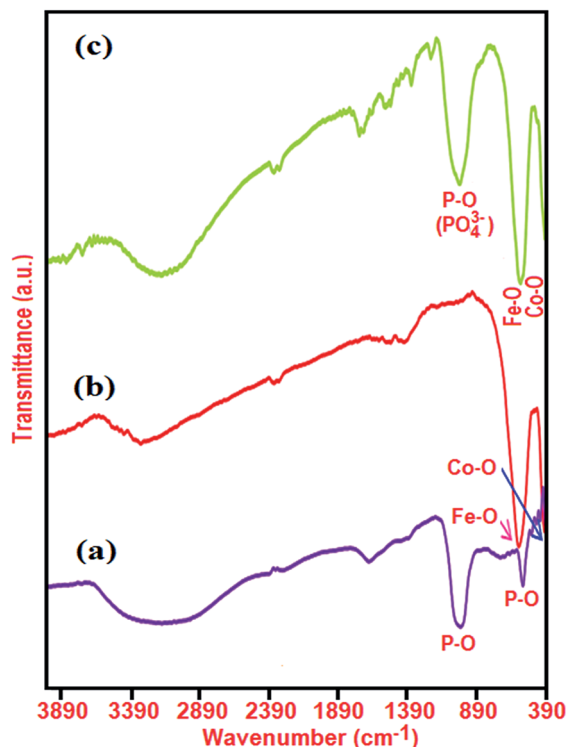
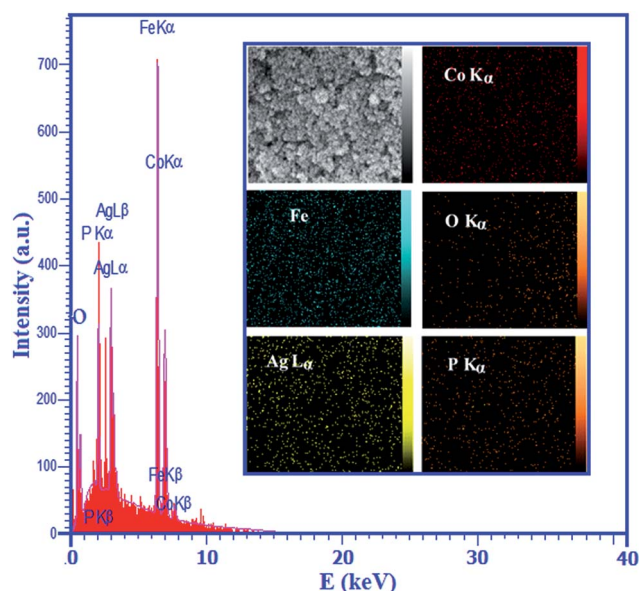**Fig. 2** IR spectra of (a) Ag_3PO_4, (b) $CoFe_2O_4$ and (c) $Ag_3PO_4/CoFe_2O_4$ nanocomposite.

Fig. 3 EDX analysis of the $Ag_3PO_4/CoFe_2O_4$ nanocomposite. The inset shows the corresponding elemental mappings of the nanocomposite.

uniformly distributed over the nanocomposite, confirming the homogeneity of the sample.

It is well known that UV-vis diffuse reflectance spectroscopy is an important characterization technique for semiconductor photocatalysts. The UV-vis diffuse reflectance spectra of the as-prepared Ag_3PO_4, $CoFe_2O_4$ and $Ag_3PO_4/CoFe_2O_4$ composite were measured and the results are shown in Fig. 4. It can be seen clearly that the pure Ag_3PO_4 and $CoFe_2O_4$ show absorption bands with absorption edges at *ca.* 530 and 500 nm, respectively (Fig. 4(a), curves i and ii). However, after coupling Ag_3PO_4 with $CoFe_2O_4$, the obtained nanocomposite material also exhibited the band with absorption edge even above 530 nm (Fig. 4(a), curve iii). Additionally, it is noted that the absorption intensity of the $Ag_3PO_4/CoFe_2O_4$ suspension was mainly enhanced in the visible region compared to that of the Ag_3PO_4, which indicates that the ability of $Ag_3PO_4/CoFe_2O_4$ to absorb visible light was increased. For the $Ag_3PO_4/CoFe_2O_4$ nanocomposite, in addition to the absorption band of Ag_3PO_4, the adsorption band of $CoFe_2O_4$ also appeared. An obvious red shift in the absorption edge of $Ag_3PO_4/CoFe_2O_4$ also occurs, in contrast to Ag_3PO_4. The band gap energy (E_g) of samples can be deducted from the formula:[38] $(\alpha h\nu)^{1/2} = B(h\nu - E_g)$, where α, ν, and B are absorption coefficient, light frequency and proportionality constant, respectively. The $(\alpha h\nu)^2$ *versus* $h\nu$ curve for the Ag_3PO_4, $CoFe_2O_4$ and $Ag_3PO_4/CoFe_2O_4$ are shown in Fig. 4(b). The value of $h\nu$ extrapolated to $\alpha = 0$ gives the absorption band gap energy.
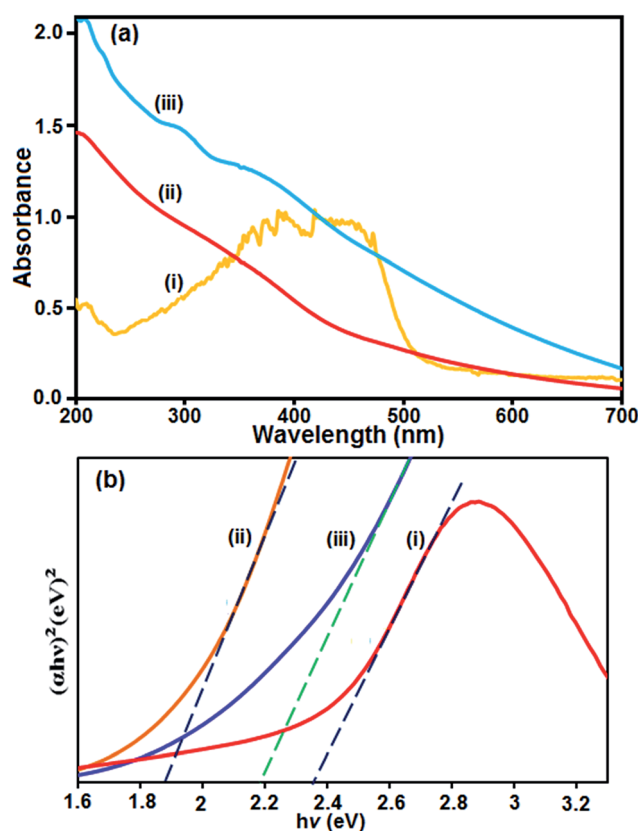

Fig. 4 (a) UV-vis absorption spectra of (i) Ag_3PO_4, (ii) $CoFe_2O_4$, and (iii) $Ag_3PO_4/CoFe_2O_4$ nanocomposite. (b) The curve of $(\alpha h\nu)^2$ *versus* ($h\nu$) for (i) Ag_3PO_4, (ii) $CoFe_2O_4$ and (iii) $Ag_3PO_4/CoFe_2O_4$ nanocomposite.

in that area. Different elements were shown in different colors in order to identify their positions within the nanomaterials. As presented in the inset of Fig. 3, the corresponding elemental mappings distribution show the existence of Ag, Co, Fe, P and O. From the maps, it can be seen that the elements are

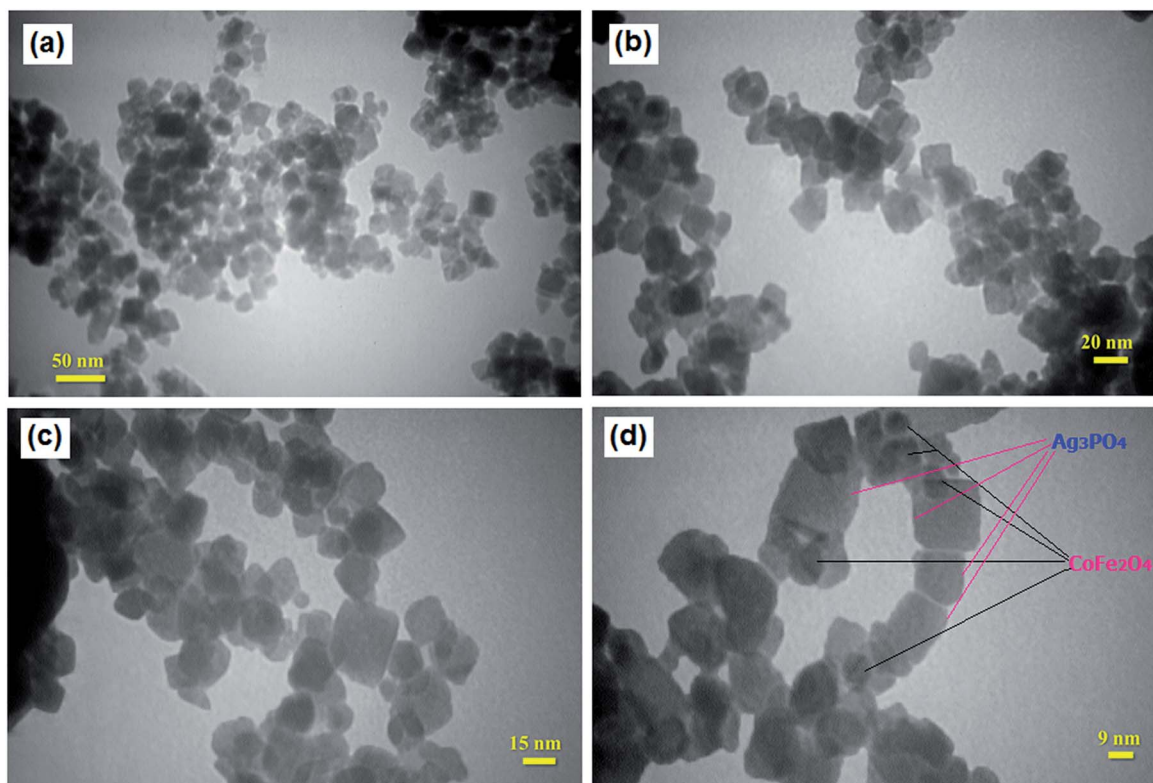**Fig. 5** TEM images of the $Ag_3PO_4/CoFe_2O_4$ nanocomposite.

From (Fig. 4(b), curves i and ii), the band gap energies for the pure Ag_3PO_4 and $CoFe_2O_4$ were estimated to be 2.36 and 1.86 eV respectively, which is in agreement with the results reported previously,[39,40] On the other hand, the band gap energy of the $Ag_3PO_4/CoFe_2O_4$ nanocomposite was found to be 2.18 eV, indicating that the introduction of $CoFe_2O_4$ decreases the E_g of Ag_3PO_4. Furthermore, the decrease of E_g upon composite formation confirms electronic coupling between Ag_3PO_4 and $CoFe_2O_4$. The visible or sunlight photocatalytic activity of $Ag_3PO_4/CoFe_2O_4$ could be attributed to the existence of this red shifted broad band.

The shape and size of the $Ag_3PO_4/CoFe_2O_4$ particles were analyzed by TEM and the images are shown in Fig. 5. As can be seen in Fig. 5(a–c), the obtained nanocomposite was formed mainly from cube-like particles. In fact, Ag_3PO_4 contains a cubic like structure with the lengths of 10–30 nm while $CoFe_2O_4$ shows a sphere-like shape. Furthermore, the high magnification TEM image in Fig. 5(d) indicates that the dark particles of $CoFe_2O_4$ with size around 10–25 nm are loaded on the surface of bright Ag_3PO_4 plates. As deduced from the TEM analysis, the particle size distribution was narrow, ranging from 10 to 30 nm, and the mean particle diameter was ~20 nm. These results were consistent with the average particle size calculated by the Debye–Scherer formula from the XRD pattern.

Fig. 6 shows the magnetic hysteresis of $CoFe_2O_4$ and $Ag_3PO_4/CoFe_2O_4$ samples at room temperature under an applied magnetic field of ± 10 kOe. It is obvious from Fig. 6, the hysteresis loops of samples are characteristic of ferromagnetic behavior. However, the magnetic saturation (M_s) of the $Ag_3PO_4/$

$CoFe_2O_4$ is lower than that of the pure $CoFe_2O_4$. From curves in Fig. 6, the M_s values for $CoFe_2O_4$ and $Ag_3PO_4/CoFe_2O_4$ were found to be 63.36 and 27.44 emu g^{-1}, respectively. In general, M_s of samples mainly depends on the content of magnetic component.[41] The content of magnetic component in the $Ag_3PO_4/CoFe_2O_4$ is less than that of pure $CoFe_2O_4$, hence, its M_s

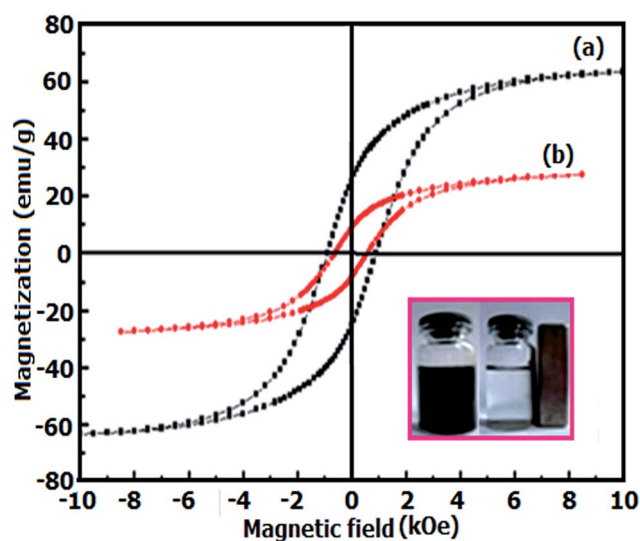**Fig. 6** Room-temperature magnetization curve as a function of applied magnetic field for (a) pure $CoFe_2O_4$ and (b) $Ag_3PO_4/CoFe_2O_4$ nanocomposite. The photo inset shows magnetically separable of the nanocomposite.

value is relatively low. However, compared with the non-magnetic Ag_3PO_4 catalyst, a magnetic $Ag_3PO_4/CoFe_2O_4$ composite catalyst can be separated from the heterogeneous reaction system by an external magnetic field as shown in the inset of Fig. 6.

3.2. Catalytic reduction of nitrophenols over $Ag_3PO_4/CoFe_2O_4$

Nitrophenols and their derivatives are some of the most refractory pollutants that occur in industrial waste water. They generally result from the production process of insecticides, synthetic dyes and herbicides.[42,43] Therefore, the removal of nitrophenols from industrial waste water is crucial for environmental health. However, nitrophenols are biologically and chemically stable compounds and it is difficult to remove them by natural microbial degradation.[44] Therefore it is necessary to develop environment friendly and clean techniques for the removal of such pollutants from industrial waste water.[45–51] In this work, the catalytic activity of the $Ag_3PO_4/CoFe_2O_4$ nanocomposite for the reduction of 4-nitrophenol (4-NP) and 2-nitrophenol (2-NP) with sodium borohydride ($NaBH_4$) was evaluated. The catalytic reduction process of 4-NP was monitored by UV-vis spectroscopy as shown in Fig. 7. It was seen that an absorption peak of 4-NP undergoes a red shift from 317 to 400 nm immediately upon the addition of aqueous solution of $NaBH_4$, corresponding to a significant change in solution color from light yellow to yellow-green due to formation of 4-nitrophenolate ion. In the absence of catalyst, the absorption peak at 400 nm remained unaltered for a long duration, indicating that the $NaBH_4$ itself cannot reduce 4-nitrophenolateion without a catalyst. In addition, the pure Ag_3PO_4 and $CoFe_2O_4$ nanoparticles show low activity in the 4-NP reduction, and therefore, they can not be regarded as effective catalysts for this reaction. However, in the presence of $Ag_3PO_4/CoFe_2O_4$ nanocomposite and $NaBH_4$, the 4-NP was easily reduced. As can be seen in Fig. 7(a), the intensity of the absorption peak of 4-NP at 400 nm decreased gradually with time and after about 24 min it approximately disappeared. In the meantime, a new absorption peak appeared at 297 nm and increased progressively in intensity. This new peak is attributed to the typical absorption of 4-aminophenol (4-AP). This result suggests that the catalytic reduction of 4-NP exclusively yielded 4-AP, without any other side products. In the reduction process, the overall concentration of $NaBH_4$ was 20 mM and 4-NP was 0.2 mM. Considering the much higher concentration of $NaBH_4$ compared to that of 4-NP, it is reasonable to assume that the concentration of BH_4^- remains constant during the reaction. In this context, pseudo-first-order kinetics could be used to evaluate the kinetic reaction rate of the current catalytic reaction, together with the UV-vis absorption data in Fig. 7(a). The absorbance of 4-NP is proportional to its concentration in solution; the absorbance at time t (A_t) and time $t = 0$ (A_0) are equivalent to the concentration at time t (C_t) and time $t = 0$ (C_0). The rate constant (k) could be determined from the linear plot of $\ln(C_t/C_0)$ *versus* reduction time in seconds. The rate constants (k) were determined from the slope of linear plots of $\ln(C_0/C)$ *versus* time (minutes); its value were determined to be 0.0098, 0.0268, and 0.0714 min^{-1}
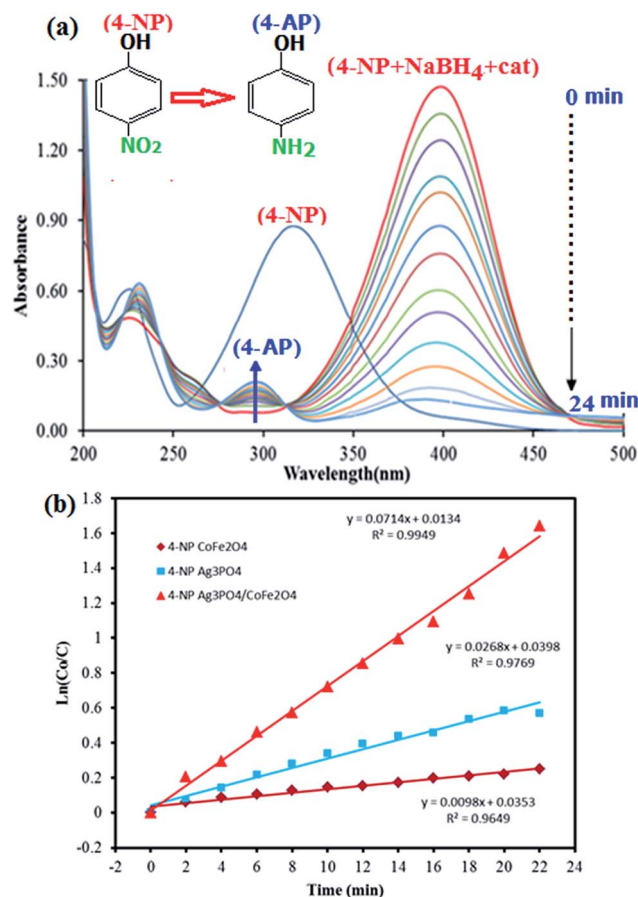

Fig. 7 (a) UV-vis spectral changes during the reduction of 4-nitrophenol (4-NP, 0.2 mM) with $NaBH_4$ (20 mM) over $Ag_3PO_4/CoFe_2O_4$ catalyst (5 mg), and (b) plot of $\ln(C_0/C_t)$ against the reaction time.

for reduction 4-NP by $CoFe_2O_4$, Ag_3PO_4 and $Ag_3PO_4/CoFe_2O_4$, respectively (Fig. 7(b)).

Fig. 8 shows the UV-vis absorption spectra of the reduction of 2-nitrophenol by $NaBH_4$ at various reaction times in the presence of $Ag_3PO_4/CoFe_2O_4$ nanocomposite. The observed peak at 414 nm for the 2-NP shows a gradual decrease in intensity with time and a new peak appeared at 291 nm indicating the formation of 2-aminophenol (2-AP). As shown in Fig. 8(b), it took 46 min for the complete reduction of 2-NP in the presence of $Ag_3PO_4/CoFe_2O_4$ nanocomposite (0.5 mg). As can be seen in Fig. 8(b), the corresponding k value was 0.0329 min^{-1} which is greater than of those of pure $CoFe_2O_4$ (0.0044 min^{-1}) and Ag_3PO_4 (0.0148 min^{-1}). The results indicated that $Ag_3PO_4/CoFe_2O_4$ exhibited considerably high activity for the reduction of nitrophenols with $NaBH_4$ as the hydrogen donor.

3.3. Photocatalytic degradation of organic dyes over $Ag_3PO_4/CoFe_2O_4$

The photocatalytic degradation of organic pollutants has attracted considerable interest because of its potential to solve serious environmental problems, such as aesthetic pollution, printing/textile wastewater, toxicity and perturbation to aquatic life, as well as making use of the unlimited and sustainable
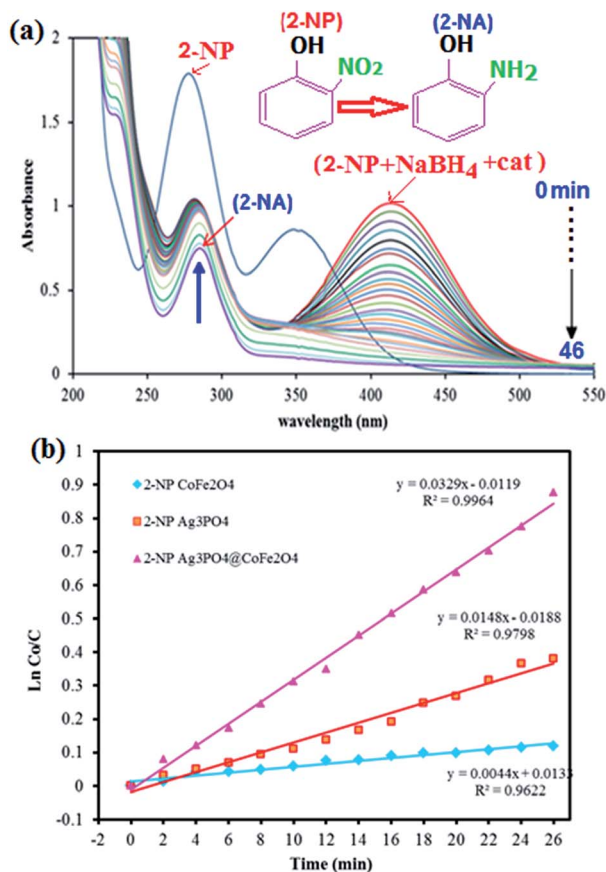
Fig. 8 (a) UV-vis spectral changes during the reduction of 2-nitro-phenol (2-NP, 0.2 mM) with NaBH$_4$ (20 mM) over Ag$_3$PO$_4$/CoFe$_2$O$_4$ catalyst (5 mg), and (b) plot of ln(C_0/C_t) against the reaction time.

energy from the sun. Various photocatalysts have been successfully developed for environmental remediation.[52] Among them, TiO$_2$ is one of the best because of its nontoxicity, acceptable stability and high photocatalytic activity.[53] However, TiO$_2$ is responsive only to UV light, which accounts for no more than 4% of the solar spectrum, greatly limiting its photo-catalytic efficiency and practical applications. Developing a novel photocatalyst with efficient sunlight or visible-light absorption and excellent stability remains a great challenge. In this regard, Ag$_3$PO$_4$/CoFe$_2$O$_4$ nanocomposite prepared in this work can be an appropriate candidate. The photocatalytic activity of magnetic Ag$_3$PO$_4$/CoFe$_2$O$_4$ nanocomposite was eval-uated by the degradation of methylene blue (MB) and Rhoda-mine B (RhB) dyes in aqueous solutions under direct sunlight irradiation and at room temperature. The UV-vis spectral changes of MB aqueous solution over Ag$_3$PO$_4$/CoFe$_2$O$_4$ photo-catalyst are plotted in Fig. 9(a) as a function of irradiation time. It shows that the intensity of maximum absorption peak of MB at 663 nm decreases dramatically as time increases and nearly disappears within 90 min. For comparison purposes, we addi-tionally performed the experiments on the degradation of MB with pure Ag$_3$PO$_4$ and CoFe$_2$O$_4$ samples under identical exper-imental conditions. As observed in Fig. 9(b), the degradation efficiency (C/C_0) of MB over CoFe$_2$O$_4$, Ag$_3$PO$_4$ and Ag$_3$PO$_4$/

CoFe$_2$O$_4$. Photocatalysts were found to be 47%, 84% and 98%, respectively, within 90 min sunlight irradiation. To understand the photocatalytic degradation kinetic of MB degradation, the pseudo-first-order model was used: ln(C_0/C) = kt, where C_0 and C are the dye concentrations before and after irradiation, respectively, k is the pseudo-first-order rate constant, and t is the reaction time. As shown in Fig. 9(c), the k values for the degradation of MB over CoFe$_2$O$_4$, Ag$_3$PO$_4$ and Ag$_3$PO$_4$/CoFe$_2$O$_4$ catalysts were determined to be 0.0052, 0.0175 and 0.0245 min^{-1}, respectively. This finding indicates that the photo-catalytic activity of Ag$_3$PO$_4$ could be improved by the incorpo-ration of CoFe$_2$O$_4$ nanoparticles.

As shown in Fig. 10, similar behavior was observed for photocatalytic degradation of RhB dye in the presence of Ag$_3$PO$_4$/CoFe$_2$O$_4$ nanocomposite and under direct sunlight irradiation. It is obvious from Fig. 10(a) that the absorption peak of RhB at 554 nm decreased significantly as time increases, indicating the efficient degradation of this cationic dye in the presence of the Ag$_3$PO$_4$/CoFe$_2$O$_4$ nanocomposite. The degrada-tion efficiency (C/C_0) of RhB over CoFe$_2$O$_4$, Ag$_3$PO$_4$ and Ag$_3$PO$_4$/CoFe$_2$O$_4$ photocatalysts was found to be 47, 80 and 100%, respectively, after 90 min sunlight irradiation (Fig. 10(b) as shown in Fig. 10(c), the pseudo-first-order rate constant (k) values for the degradation of MB over CoFe$_2$O$_4$, Ag$_3$PO$_4$ and Ag$_3$PO$_4$/CoFe$_2$O$_4$ catalysts were determined to be 0.0059, 0.0149 and 0.0266 min^{-1}, respectively.

In photocatalytic degradation, some active species, including hydroxyl radicals (·OH), superoxide anion radicals (·O$_2^-$), photogenerated holes (h$^+$) and electrons (e$^-$), are formed by light irradiation.[54,55] To determine which active species play an important role in dye photodegradation using Ag$_3$PO$_4$/CoFe$_2$O$_4$ under sunlight irradiation, a series of experiments on quenching active species was conducted by adding individual scavengers to the photocatalytic reaction system. The different scavengers used in this study were BQ (·O$_2^-$ quencher), TEA (h$^+$ quencher), IPA (·OH quencher), KI (h$^+$ and ·OH quencher) and Ag$^+$ (e$^-$ quencher) during MB degradation.

As a consequence of quenching, the photocatalytic reaction is partly inhibited and leads to low MB conversion. The extent of decrease caused by scavengers in the conversion indicated the importance of the corresponding reactive species.

The effects of the series of scavengers were evaluated by comparing the degradation extents of MB under sunlight irra-diation. Fig. 11 shows that RhB photodegradation using Ag$_3$PO$_4$/CoFe$_2$O$_4$ is greatly suppressed after adding BQ as ·O$_2^-$ scavenger, which suggests that ·O$_2^-$ is the main reactive species in the photocatalytic process. When TEA, IPA or KI are added, the photodegradation activity of Ag$_3$PO$_4$/CoFe$_2$O$_4$ slightly decreases, which indicates that h$^+$ and ·OH play a minor but synergistic role. The addition of AgNO$_3$ has a moderate effect, which implies that e$^-$ is reactive but is not the significant active species in the photocatalytic reaction. In summary, the main reactive species involved in MB degradation over Ag$_3$PO$_4$/CoFe$_2$O$_4$ is ·O$_2^-$, with e$^-$, h$^+$ and ·OH also being generated during the photocatalytic reaction under direct sunlight irradiation.
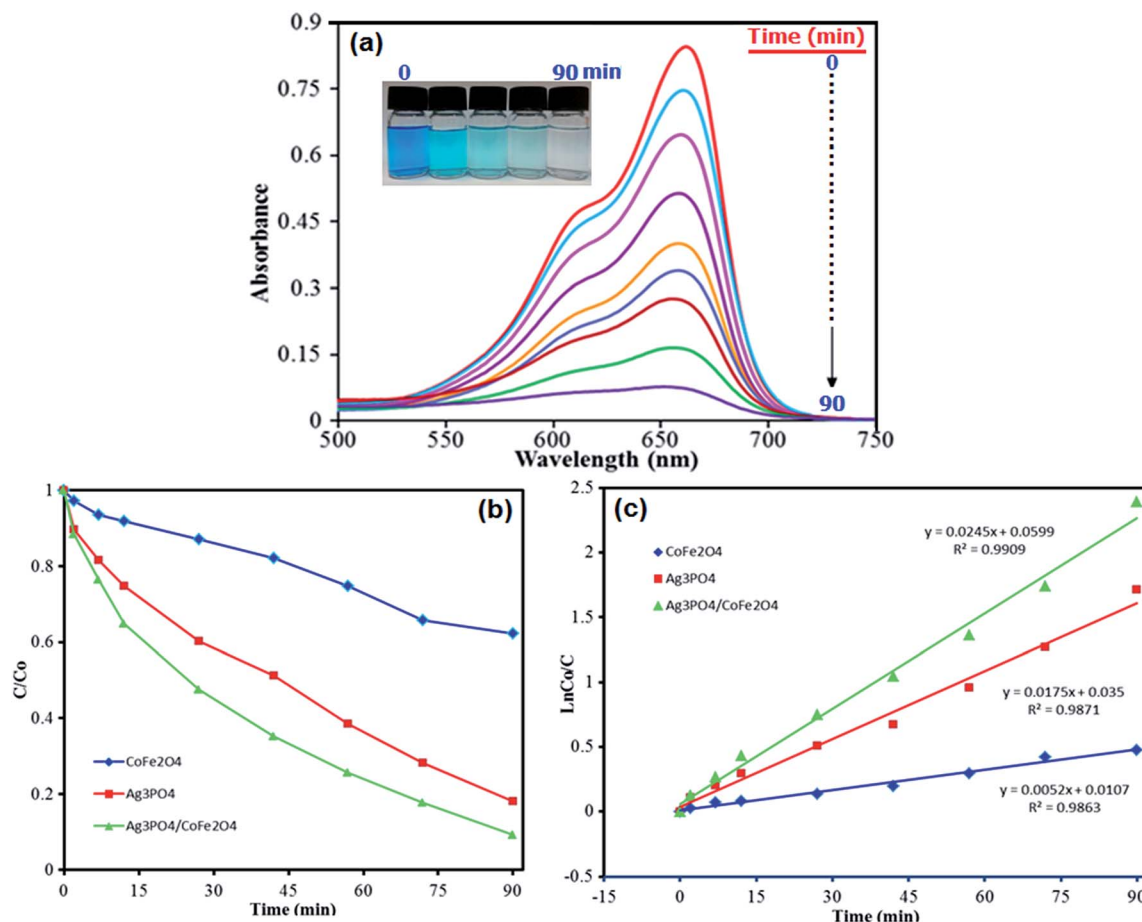
Fig. 9 (a) UV-vis spectral changes of MB aqueous solution over $Ag_3PO_4/CoFe_2O_4$ under sunlight irradiation at different time intervals, (b) concentration changes of MB as a function of irradiation time. (c) Plot of $\ln(C_0/C)$ vs. irradiation time. Conditions: [MB] = 50 mL, 15 mg L^{-1}; [photocatalyst] = 25 mg/50 mL at 25 °C.

The general principle for the enhanced photocatalytic performance of nanocomposite photocatalysts is that they have different electronic energy levels so that charge separation can be enhanced. In order to understand the band structure of $Ag_3PO_4/CoFe_2O_4$ nanocomposite, the potentials of the conduction band (CB) and valence band (VB) edges of Ag_3PO_4 and $CoFe_2O_4$ were calculated according to the Mulliken electronegativity theory, which is shown as follow in eqn (1) and (2):

$$E_{VB} = \chi - E_C + 0.5E_g \qquad (1)$$

$$E_{CB} = E_{VB} - E_g, \qquad (2)$$

where E_{VB} and E_{CB} stand for the conduction band and valence band edge potential respectively, χ is the absolute electronegativity of the semiconductor, which is the geometric mean of the electronegativities of the constituent atoms,[56] and E_c is the energy of free electrons on the hydrogen scale (about 4.5 eV vs. NHE),[57] Eg is the band gap of semiconductor. The χ value is calculated to be 5.92 eV for Ag_3PO_4 and 5.47 eV for $CoFe_2O_4$, respectively. The calculated E_{CB} and E_{VB} edge positions for Ag_3PO_4 are 0.49 and 2.85 eV, and for $CoFe_2O_4$ are 0.14 and 1.9 eV, respectively, which are close to previous reported values.[58,59]

On the basis of the above results and the detection of active species in the photodegradation process, a possible photocatalytic mechanism for dye photodegradation using $Ag_3PO_4/CoFe_2O_4$ nanocomposite has been proposed as follows and illustrated in Fig. 12.[60–64] Under irradiation with sunlight, both $CoFe_2O_4$ and the Ag_3PO_4 can absorb the photon energy and produce the electron–hole pairs (eqn (3)). Since, the flat band potential of $CoFe_2O_4$ is more negative than that of Ag_3PO_4, the electrons keep transferring from $CoFe_2O_4$ to Ag_3PO_4 until the Fermi level equilibrium of both is attained. Meanwhile, photoinduced holes from valence band (VB) of Ag_3PO_4 would be immigrated to the less positive VB of $CoFe_2O_4$ and further reacted with the absorbed H_2O molecules or hydroxyl ion (OH^-) to form active oxidants such as hydroxyl radicals ($^•OH$) (eqn (4)). At the same time, the accumulated electrons on the surface of Ag_3PO_4 reacts with absorbed oxygen to form oxidants such as superoxide ions ($^•O_2^-$) (eqn (5)). Therefore, the generated active species, such as $^•O_2^-$, h^+ and $^•OH$, effectively react to degrade the dye molecules to CO_2, H_2O or other products (eqn (6)). The proposed mechanism of photocatalytic dye degradation using $Ag_3PO_4/CoFe_2O_4$ heterostructure can be described as follows:

$$Ag_3PO_4/CoFe_2O_4 + sunlight \rightarrow e_{CB(Ag_3PO_4)}^{-} + h_{VB(CoFe_2O_4)}^{+} \quad (3)$$
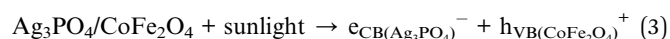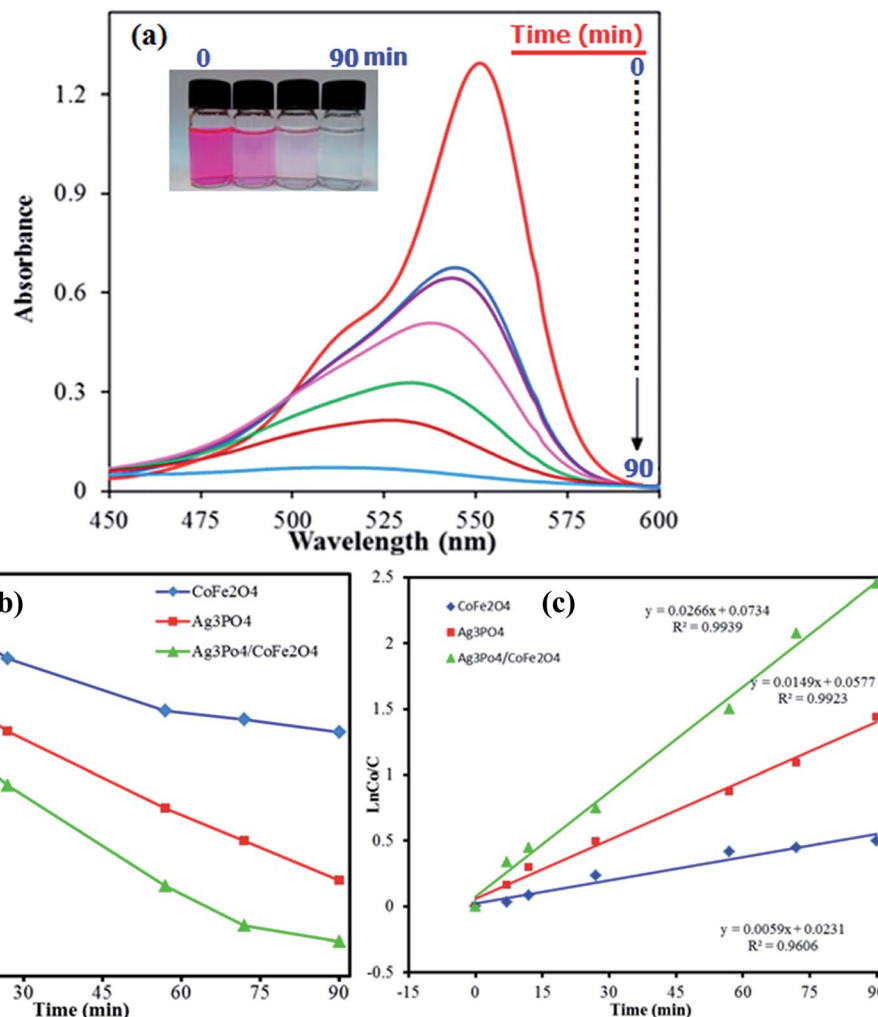
Fig. 10 (a) UV-vis spectral changes of RhB aqueous solution over $Ag_3PO_4/CoFe_2O_4$ under sunlight irradiation at different time intervals, (b) concentration changes of RhB as a function of irradiation time. (c) Plot of $\ln(C_0/C)$ *vs.* irradiation time. Conditions: [RhB] = 50 mL, 15 mg L^{-1}; [photocatalyst] = 25 mg/50 mL at 25 °C.
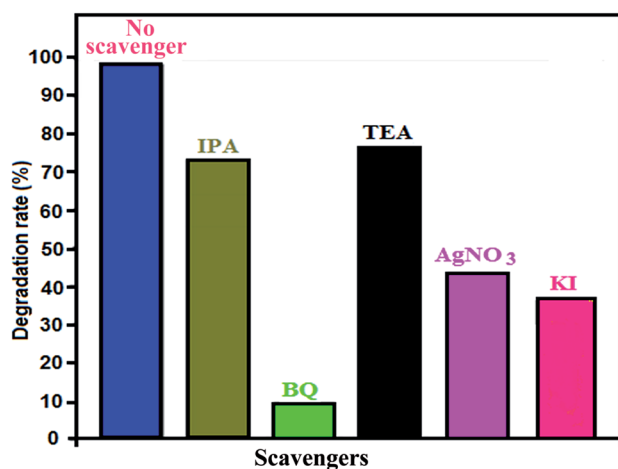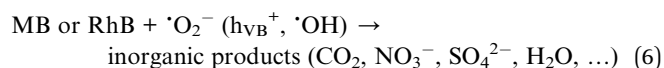

Fig. 11 Effects of various active scavengers on the degradation of MB over $Ag_3PO_4/CoFe_2O_4$ nanocomposite under irradiation with sunlight.

$$h_{VB}^+ + H_2O/OH^- \rightarrow {}^{\bullet}OH + H^+ \qquad (4)$$

$$e_{CB}^- + O_2 \rightarrow {}^{\bullet}O_2^- \qquad (5)$$

$$\begin{aligned} MB \text{ or } RhB + {}^{\bullet}O_2^- \ (h_{VB}^+, {}^{\bullet}OH) \rightarrow \\ \text{inorganic products } (CO_2, NO_3^-, SO_4^{2-}, H_2O, \ldots) \end{aligned} \qquad (6)$$

According to the above-suggested mechanism, electrons in the CB of $CoFe_2O_4$ can migrate to the CB of Ag_3PO_4 because the interfacial contact formed between $CoFe_2O_4$ and Ag_3PO_4 effectively hinders the recombination of electron–hole pairs and thus enhances photodegradation efficiency, compared to those of pure Ag_3PO_4 and $CoFe_2O_4$.

Furthermore, RhB and MB dyes demonstrate the strong absorption bands in the visible region at wavelengths of 552 and 663 nm. Therefore, they can undergo photosensitization under visible sunlight irradiation. The mechanism of indirect dye photosensitization induced degradation on the nanocomposite can be explained in the following procedure.[65,66] First, the dye
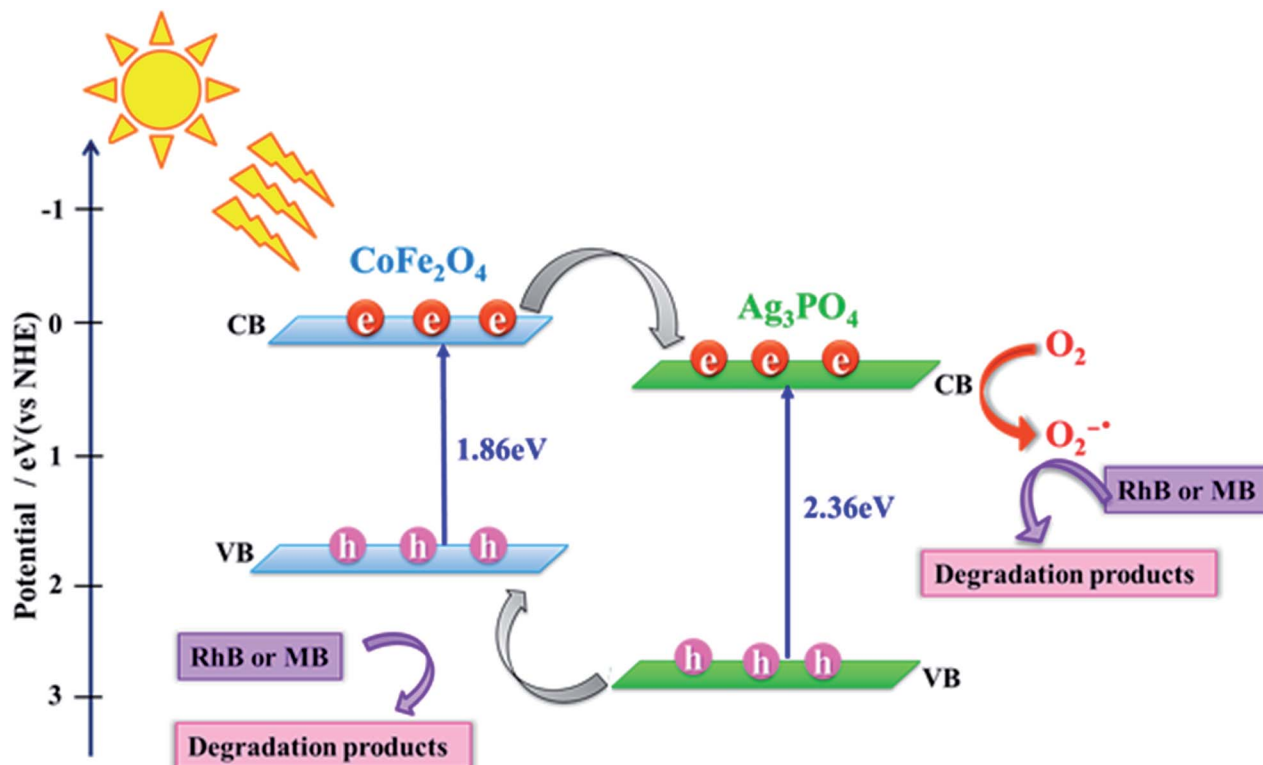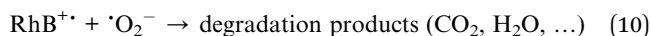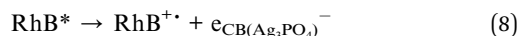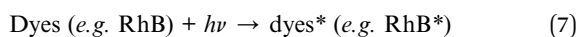
Fig. 12 A proposed mechanism for photocatalytic degradation of dyes over $Ag_3PO_4/CoFe_2O_4$ nanocomposite under direct sunlight irradiation.

molecules (*e.g.* RhB) are absorbed on the surface of nano-composite and then transferred into its excited state (RhB*) under sunlight irradiation (eqn (7)). Second, the electrons are injected from the RhB* into the conduction band of the Ag_3PO_4 where the electrons are trapped by the molecules' oxygen (eqn (8) and (9)). Third, the electrons in the CB of Ag_3PO_4 react with O_2 to produce $^{\bullet}O_2^{-}$ radicals for further degradation of $RhB^{+\bullet}$ (eqn (10)). In fact, the $Ag_3PO_4/CoFe_2O_4$ is served only as an electron-mediator, which may be favorable for the effective separation and transfer of the injected electrons and cationic RhB radicals. Thus, the photo-generated electrons in the excited dyes and molecular oxygen play a crucial role in the indirect dye photosensitization pathway.

$$\text{Dyes } (e.g. \text{ RhB}) + h\nu \rightarrow \text{dyes* } (e.g. \text{ RhB*}) \tag{7}$$

$$\text{RhB*} \rightarrow \text{RhB}^{+\bullet} + e_{CB(Ag_3PO_4)}^{-} \tag{8}$$

$$e_{CB}^{-} + O_2 \rightarrow {}^{\bullet}O_2^{-} \tag{9}$$

$$\text{RhB}^{+\bullet} + {}^{\bullet}O_2^{-} \rightarrow \text{degradation products } (CO_2, H_2O, \ldots) \tag{10}$$

3.4. Reusability and photostability tests

To evaluate the reusability and photostability of the $Ag_3PO_4/CoFe_2O_4$ nanocomposite catalyst, recycling experiments were performed. It was separated from the reaction mixture after its first use in the degradation of MB. The recovered catalyst was found to be reusable for five runs without significant loss in activity. As shown in Fig. 13, nearly 7% of decrease could be observed after four times recycle. For each recycle, the centri-fuge supernatant was collected and analyzed by Atomic Absorption Spectroscopy. It was shown that no silver metal signal during the course of the recycling reaction, confirming the stability of the catalyst.

Furthermore, the structural stability the recovered $Ag_3PO_4/CoFe_2O_4$ photocatalyst was confirmed by XRD and FT-IR after five runs (Fig. 14). As shown in Fig. 14(a) and (b), XRD pattern

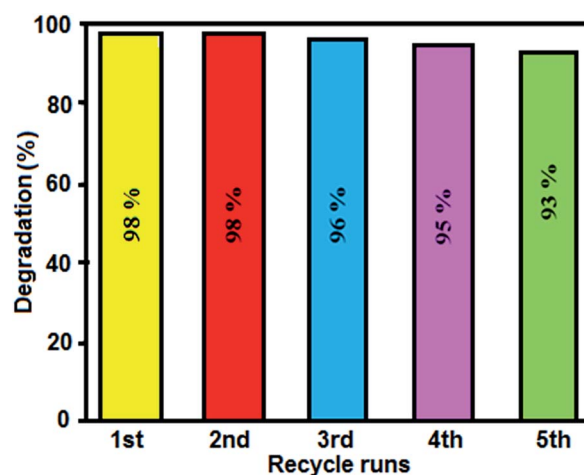**Fig. 13** Recyclability of the $Ag_3PO_4/CoFe_2O_4$ nanocomposite in the photodegradation of MB under sunlight irradiation.

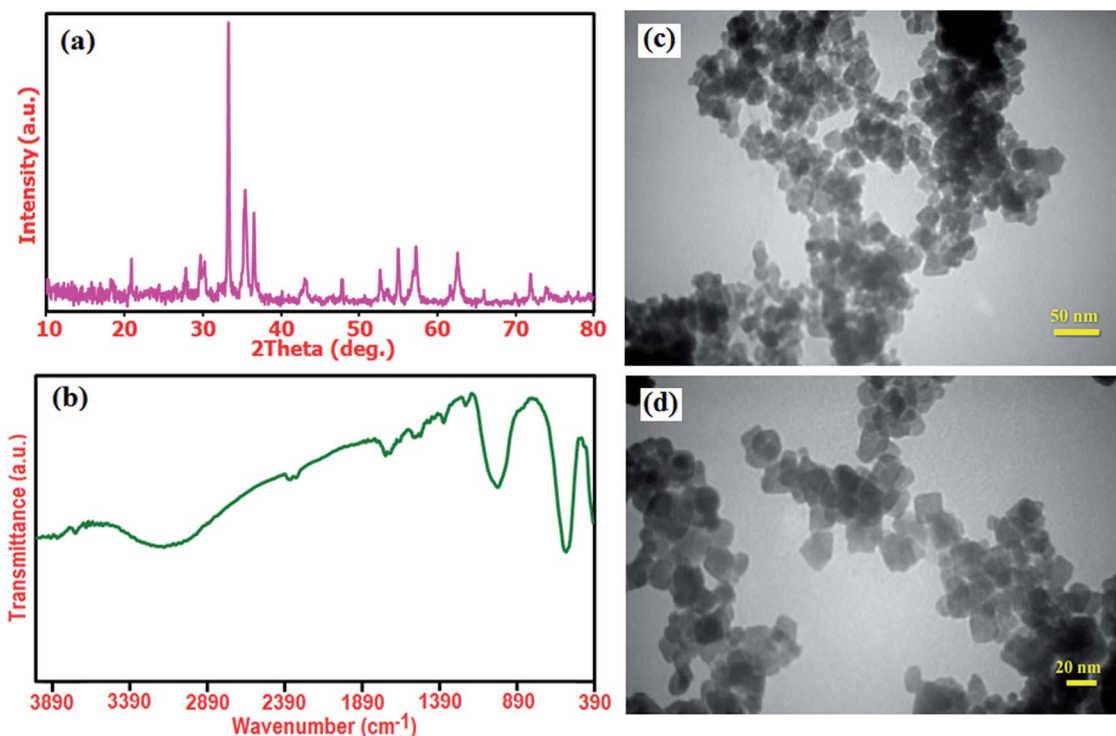**Fig. 14** (a) XRD pattern, (b) FT-IR spectrum, (c) and (d) TEM images of the recovered $Ag_3PO_4/CoFe_2O_4$ photocatalyst after five runs of catalytic reaction.

and FT-IR spectrum of the recovered photocatalyst did not show significant change after the fifth run in comparison with those of the fresh catalyst (see Fig. 1(c) and 2(c)). These observations confirm that the structure of the $Ag_3PO_4/CoFe_2O_4$ nanocomposite is stable under the reaction conditions and was not affected by the reactants. The morphology of the recycled $Ag_3PO_4/CoFe_2O_4$ photocatalyst particles after several runs of catalytic degradation of MB was also analyzed. Fig. 14(d) and (c) show two representative TEM images of the $Ag_3PO_4/CoFe_2O_4$ photocatalyst after 5 cycles of catalytic reaction. It could be observed that the recovered catalyst almost kept initial size and morphology (see Fig. 6) even after five runs of catalytic reaction. The surface of individual cubic Ag_3PO_4 particles is still decorated with $CoFe_2O_4$, revealing the strong binding between the $CoFe_2O_4$ nanoparticles and cubic Ag_3PO_4 particles.

4. Conclusions

In summary, we have presented a facile method for the synthesis of novel magnetic $Ag_3PO_4/CoFe_2O_4$ nanocomposite through the hydrothermal method. Compared with the pure Ag_3PO_4 and $CoFe_2O_4$, the $Ag_3PO_4/CoFe_2O_4$ exhibited superior activity reduction 2- and 4-NP. Also, the nanocomposite was used to degrade MB and RhB organic dyes pollutants under sunlight. Because the efficient separation of electron–hole pairs, the photocatalytic activity of $Ag_3PO_4/CoFe_2O_4$ is higher than that of pure Ag_3PO_4 and $CoFe_2O_4$. Furthermore, the $Ag_3PO_4/CoFe_2O_4$ nanocatalyst could be easily separated from wastewater for reuse by simply applying an external magnetic

field. This study provides a green, low-cost, simple and rapid procedure for the degradation of organic dyes pollutants in aqueous wastewater solutions by using solar energy.

References

1 N. S. Lewis and D. G. Nocera, *Proc. Natl. Acad. Sci. U. S. A.*, 2006, **103**, 15729–15735.
2 N. S. Lewis, *Science*, 2007, **315**, 798–801.
3 M. N. Chong, B. Jin, C. W. K. Chow and C. Saint, *Water Res.*, 2010, **44**, 2997–3027.
4 M. Ni, M. K. H. Leung, D. Y. C. Leung and K. Sumathy, *Renewable Sustainable Energy Rev.*, 2007, **11**, 401–425.
5 X. Y. Guo, C. F. Chen, S. Y. Yin, L. J. Huang and W. P. Qin, *J. Alloys Compd.*, 2015, **619**, 293–297.
6 B. Liu, Y. Fang, Z. Li and S. Xu, *J. Nanosci. Nanotechnol.*, 2015, **15**, 889–920.
7 P. V. Kamat, *Chem. Rev.*, 1993, **93**, 267–300.
8 Z. Yi, J. Ye, N. Kikugawa, T. Kako, S. Ouyang, H. Stuart-Williams, H. Yang, J. Cao, W. Luo, Z. Le, Y. Liu and R. Withers, *Nat. Mater.*, 2010, **9**, 559–564.
9 Y. Bi, S. Ouyang, N. Umezawa, J. Cao and J. Ye, *J. Am. Chem. Soc.*, 2011, **133**, 6490–6492.

10 W. Yao, B. Zhang, C. Huang, C. Ma, X. Song and Q. Xu, *J. Mater. Chem.*, 2012, **22**, 4050–4055.

11 S. B. Rawal, S. D. Sung and W. I. Lee, *Catal. Commun.*, 2012, **17**, 131–135.

12 J. Q. Zhang, K. Yu, Y. F. Yu, L. L. Lou, Z. Q. Yang, J. W. Yang and S. X. Liu, *J. Mol. Catal. A: Chem.*, 2014, **391**, 12–18.

13 Z. M. Yang, G. F. Huang, W. Q. Huang, J. M. Wei, X. G. Yan, Y. Y. Liu, C. Jiao, Z. Wan and A. L. Pan, *J. Mater. Chem. A*, 2014, **2**, 1750–1756.

14 X. J. Guan and L. J. Guo, *ACS Catal.*, 2014, **4**, 3020–3026.

15 J. Guo, S. Ouyang, P. Li, Y. Zhang, T. Kako and J. H. Ye, *Appl. Catal., B*, 2013, **134**, 286–292.

16 J. J. Guo, S. X. Ouyang, H. Zhou, T. Kako and J. H. Ye, *J. Phys. Chem. C*, 2013, **117**, 17716–17724.

17 B. C. Cao, P. Y. Dong, S. Cao and Y. H. Wang, *J. Am. Ceram. Soc.*, 2013, **96**, 544–548.

18 C. J. Li, P. Zhang, R. Lv, J. W. Lu, T. Wang, S. P. Wang, H. F. Wang and J. L. Gong, *Small*, 2013, **9**, 3951–3956.

19 Y. H. Song, H. Xu, C. Wang, J. J. Chen, J. Yan, Y. G. Xu, Y. P. Li, C. B. Liu, H. M. Li and Y. C. Lei, *RSC Adv.*, 2014, **4**, 56853–56862.

20 H. Katsumata, T. Sakai, T. Suzuki and S. Kaneco, *Ind. Eng. Chem. Res.*, 2014, **53**, 8018–8025.

21 F. J. Zhang, F. Z. Xie, S. F. Zhu, J. Liu, J. Zhang, S. F. Mei and W. Zhao, *Chem. Eng. J.*, 2013, **228**, 435–441.

22 J. T. Tang, W. Gong, T. J. Cai, T. Xie, C. Deng, Z. S. Peng and Q. Deng, *RSC Adv.*, 2013, **3**, 2543–2547.

23 W. Liu, M. L. Wang, C. X. Xu, S. F. Chen and X. L. Fu, *Mater. Res. Bull.*, 2013, **48**, 106–113.

24 L. Zhang, H. Zhang, H. Huang, Y. Liu and Z. Kang, *New J. Chem.*, 2012, **36**, 1541–1544.

25 C. Tang, E. Liu, J. Fan, X. Hu, L. Kang and J. Wan, *Ceram. Int.*, 2014, **40**, 15447–15453.

26 X. L. Ma, H. H. Li, Y. H. Wang, H. Li, B. Liu, S. Yin and T. Sato, *Appl. Catal., B*, 2014, **158**, 314–320.

27 P. Amornpitoksuk and S. Suwanboon, *Adv. Powder Technol.*, 2014, **25**, 1026–1030.

28 P. Amornpitoksuk and S. Suwanboon, *Adv. Mater. Res.*, 2014, **970**, 29–32.

29 R. Shao, X. Zeng, Z. Cao, H. Dong, L. Wang, F. Wang, J. Liu, Z. Li and Q. Liang, *RSC Adv.*, 2015, **5**, 102101–102107.

30 Y. K. Jo, I. Y. Kim, J. M. Lee, S. Nahm, J. W. Choi and S. J. Hwang, *Mater. Lett.*, 2014, **114**, 152–155.

31 G. Xi, B. Yue, J. Cao and J. Ye, *Chem.–Eur. J.*, 2011, **17**, 5145–5154.

32 M. M. Ye, Q. Zhang, Y. X. Hu, J. P. Ge, Z. D. Lu, L. He, Z. L. Chen and Y. D. Yin, *Chem.–Eur. J.*, 2010, **16**, 6243–6250.

33 Y. M. Moustafa and K. El-Egili, *J. Non-Cryst. Solids*, 1998, **240**, 144–153.

34 S. Q. Huang, Y. G. Xu, M. Xie, H. Xu, M. Q. He, J. X. Xia, L. Y. Huang and H. M. Li, *Colloids Surf., A*, 2015, **478**, 71–80.

35 N. Adeela, K. Maaz, U. Khan, S. Karim, A. Nisar, M. Ahmad, G. Ali, X. F. Han, J. L. Duan and J. Liu, *J. Alloys Compd.*, 2015, **639**, 533–540.

36 N. Quandt, R. Roth, F. Syrowatka, M. Steimecke and S. G. Ebbinghaus, *J. Solid State Chem.*, 2016, **233**, 82–89.

37 R. Kurchania, D. Rathore and R. K. Pandey, *J. Mater. Sci.: Mater. Electron.*, 2015, **26**, 9355–9365.

38 Z. Jiao, Y. Zhang, H. Yu, G. Lu, J. Ye and Y. Bi, *Chem. Commun.*, 2013, **49**, 636–638.

39 Z. G. Yi, J. H. Ye, N. Kikugawa, T. Kako, S. X. Ouyang, H. Stuart-Williams, H. Yang, J. Y. Cao, W. J. Luo, Z. S. Li, Y. Liu and R. L. Withers, *Nat. Mater.*, 2010, **9**, 559–564.

40 Y. Fu and X. Wang, *Ind. Eng. Chem. Res.*, 2011, **50**, 7210–7218.

41 I. Lascu, S. K. Banerjee and T. S. Berquó, *Geochem., Geophys., Geosyst.*, 2010, **11**, 1–22.

42 F. K. Higson, *Adv. Appl. Microbiol.*, 1992, **37**, 1–19.

43 M. J. Vaidya, S. M. Kulkarni and R. V. Chaudhari, *Org. Process Res. Dev.*, 2003, **27**, 202–208.

44 A. H. Abbar, A. H. Sulaymon and M. G. Jalhoom, *Electrochim. Acta*, 2007, **53**, 1671–1679.

45 Y. Du, H. L. Chen, R. Z. Chen and N. P. Xu, *Appl. Catal., A*, 2004, **277**, 259–264.

46 K. Polat, M. Aksu and A. Pekel, *J. Appl. Electrochem.*, 2002, **32**, 217–223.

47 M. Nasrollahzadeh, S. M. Sajadi, A. Rostami-Vartooni and M. Khalaj, *J. Mol. Catal. A: Chem.*, 2015, **396**, 31–39.

48 M. Nasrollahzadeh, S. M. Sajadi, A. Rostami-Vartooni, M. Alizadeh and M. Bagherzadeh, *J. Colloid Interface Sci.*, 2016, **466**, 360–368.

49 A. Rostami-Vartooni, M. Nasrollahzadeh, M. Salavati-Niasari and M. Atarod, *J. Alloys Compd.*, 2016, **689**, 15–20.

50 M. Nasrollahzadeh, M. Bagherzadeh and H. Karimi, *J. Colloid Interface Sci.*, 2016, **465**, 271–278.

51 Q. Geng and J. Du, *RSC Adv.*, 2014, **4**, 16425–16428.

52 M. J. Sevrin, C. R. J. Stephenson and J. J. Douglas, *Org. Process Res. Dev.*, 2016, **20**, 1134–1147.

53 Y. Bai, I. Mora-Seró, F. D. Angelis, J. Bisquert and P. Wang, *Chem. Rev.*, 2014, **114**, 10095–10130.

54 K. Yu, S. Yang, C. Liu, H. Chen, H. Li, C. Sun and S. A. Boyd, *Environ. Sci. Technol.*, 2012, **46**, 7318–7326.

55 H. Zhang, X. Lv, Y. Li, Y. Wang and J. Li, *ACS Nano*, 2010, **4**, 380–386.

56 X. Xin, J. Y. Lang, T. T Wang, Y. G. Su, Y. X. Zhao and X. J. Wang, *Appl. Catal., B*, 2016, **181**, 197–209.

57 Y. G. Su, X. Xin, Y. F. Wang, T. T. Wang and X. J. Wang, *Chem. Commun.*, 2014, **50**, 4200–4202.

58 M. Ge, N. Zhu, Y. Q. Zhao, J. Li and L. Liu, *Ind. Eng. Chem. Res.*, 2012, **51**, 5167–5173.

59 Y. I. Choi, Y. I. Kim, D. W. Cho, J. S. Kang, K. T. Leung and Y. Sohn, *RSC Adv.*, 2015, **5**, 79624–79634.

60 G. Li and L. Mao, *RSC Adv.*, 2012, **2**, 5108–5111.

61 D. Zhang and F. Zeng, *J. Mater. Sci.*, 2012, **47**, 2155–2161.

62 S. S. Patil, M. G. Mali, M. S. Tamboli, D. R. Patil, M. V. Kulkarni, H. Yoon, H. Kim, S. S. Al-Deyab, S. S. Yoon, S. S. Kolekar and B. B. Kale, *Catal. Today*, 2015, **260**, 126–134.

63 S. Zhang, J. Li, H. Niu, W. Xu, J. Xu, W. Hu and X. Wang, *ChemPhysChem*, 2013, **78**, 192–199.

64 D. Guo, R. Wen, M. Liu, H. Guo, J. Chen and W. Weng, *Appl. Organomet. Chem.*, 2015, **29**, 690–697.

65 J. Jiang, K. Zhao, X. Y. Xiao and L. Z. Zhang, *J. Am. Chem. Soc.*, 2012, **134**, 4473–4476.

66 J.-M. Wu and T.-W. Zhang, *J. Photochem. Photobiol., A*, 2004, **162**, 171–177.